Quantifying Seismic Properties of a River Channel at Mount Rainier for Use in Debris Flow Monitoring and Analysis

Avery E. Conner*[1], Amanda M. Thomas[1,2], Kate E. Allstadt[3], Weston A. Thelen[4], Elaine Collins[3], Maxime Farin[5], William J. Stephenson[3], Alexandra M. Iezzi[4], and Katherine M. Biegel[1,2]

Abstract

Theoretical models that relate debris flow properties to their seismic signature suggest seismic methods may be used to remotely characterize properties of these events. However, the complexity of debris flow sources and poorly constrained material properties in near-surface environments limit our ability to determine important attributes of debris flows, such as volume and particle size distribution, from seismic records alone. In this study, we explore the sensitivity of debris flow seismic signals to subsurface seismic characteristics using an established debris flow seismicity model and subsurface properties derived from active-source measurements in the Tahoma Creek stream channel at Mount Rainier, United States. Using refraction and multichannel analysis of surface waves, we estimate 1D primary and secondary wave velocity profiles to a depth of 11 m and calculate the frequency-varying phase velocity (v_c) and Rayleigh-wave quality factor (Q_R) for frequencies between 9 and 50 Hz. We find that the Tahoma Creek stream channel has low v_c, varying with frequency between 226 and 434 m/s, and is highly attenuating, with Q_R estimated below 13.3 at all analyzed frequencies. We model the seismic signal of a hypothetical debris flow in Tahoma Creek using our measured values and compare the results against the same model but varying v_c and Q_R over a range of frequency-independent, single values commonly used in the literature when measurements are not available ($v_c = 250$–750 m/s, $Q_R = 3$–33). We find that the power spectral densities of the modeled debris flows vary by orders of magnitude within the subset of our test values, highlighting the benefits of measuring material properties when using modeled debris flow seismic signals for quantitative monitoring.

Cite this article as Conner, A. E., A. M. Thomas, K. E. Allstadt, W. A. Thelen, E. Collins, M. Farin, W. J. Stephenson, A. M. Iezzi, and K. M. Biegel (2026). Quantifying Seismic Properties of a River Channel at Mount Rainier for Use in Debris Flow Monitoring and Analysis, *Seismol. Res. Lett.* **XX**, 1–15, doi: 10.1785/0220250071.

Supplemental Material

Introduction

Debris flows are common natural hazards consisting of channelized flows of water-saturated materials that occur in areas with steep relief and a sufficient influx of water (Iverson, 1997; Hungr *et al.*, 2001). Depending on the location and characteristics of the flow, materials such as sand, gravel, cobbles, boulders, and organic material may be carried tens of kilometers at velocities that may reach or occasionally exceed 10 m/s (Iverson, 1997; Hungr *et al.*, 2001). Debris flows have historically caused extensive destruction around the world, particularly in volcanic settings, in which they are commonly called lahars (Jakob and Hungr, 2005; Witham, 2005). The events often start in remote locations, making ground-motion sensors, like seismometers, ideal for monitoring debris flows because the instruments can provide near real-time information even at distances up to tens of kilometers.

Debris flows generate seismic waves by producing normal and shear forces through agitated particles interacting with adjacent particles and the channel bed (Allstadt *et al.*, 2020). The particles bounce, roll, or slide, dissipating energy with each collision to generate the high-frequency (> 1 Hz) energy that dominates the debris flow seismic signature (Iverson, 1997; Allstadt *et al.*, 2018, 2020). Efforts have been made in recent years to interpret debris flow characteristics from recorded seismic waves to better understand how

1. Department of Earth Sciences, University of Oregon, Eugene, Oregon, U.S.A., https://orcid.org/0000-0001-8682-6169 (KMB); 2. Department of Earth and Planetary Sciences, University of California, Davis, California, U.S.A.; 3. U.S. Geological Survey, Geologic Hazards Science Center, Golden, Colorado, U.S.A., https://orcid.org/0000-0003-4977-5248 (KEA); https://orcid.org/0000-0002-5475-4022 (EC); https://orcid.org/0000-0001-8699-0786 (WJS); 4. U.S. Geological Survey, Volcano Science Center, Cascades Volcano Observatory, Vancouver, Washington, U.S.A., https://orcid.org/0000-0003-2534-5577 (WAT); 5. HYGEOS, Lille, France

*Corresponding author: aconner2@uoregon.edu

debris flows develop and evolve, as well as establish early warning systems for regions prone to the events (e.g., Arattano and Marchi, 2008; Hürlimann *et al.*, 2019; Kramer *et al.*, 2024; Marchi *et al.*, 2024). Focus has gone into relating debris flow parameters like volume, particle diameter, and velocity to seismic signals because these attributes correlate strongly with the hazard potential of the flow (e.g., Allstadt *et al.*, 2018; Lai *et al.*, 2018; Zhang *et al.*, 2021; Schimmel *et al.*, 2022). Models that link reported or estimated flow properties to the high-frequency energy of flow-type events typically consider the energy source to be individual, random impacts from particles with a statistical size distribution determined by bulk flow properties (e.g., Tsai *et al.*, 2012; Farin *et al.*, 2019). The models show promise in some cases for estimating reasonable values for debris flow properties such as erosion rates (Kean *et al.*, 2015) and particle diameter (Zhang *et al.*, 2021). In particular, Farin *et al.* (2019) developed an analytic model allowing individual sections of a debris flow to have different particle size distributions, providing additional opportunities to investigate how debris flow structure influences the seismic signature.

Despite advancements in debris flow modeling, uncertainties remain surrounding how seismic waves are generated by flow sources, and the complexity of the recorded seismic signals has confounded efforts to fully develop the necessary theory (Allstadt *et al.*, 2020). Both modeling and analysis of observed debris flow seismic signals depend on path effects that are often poorly constrained in near-source environments, especially in complex volcanic environments in which large and damaging debris flows are more common (Vallance, 2005; Allstadt *et al.*, 2018). River channels and volcanoes are highly attenuating environments (e.g., Petrosino *et al.*, 2002; Jolly *et al.*, 2012), causing recorded debris flow seismic waves to have lower amplitude and lower power in high frequencies than may be predicted by models.

In this study, we examine the path-effect problem by performing an active source experiment in the Tahoma Creek stream channel (Fig. 1) on Mount Rainier, an active stratovolcano in the Cascade Range of North America. We quantify near-surface 1D primary wave (*P*-wave) and secondary wave (*S*-wave) velocity structures as well as Rayleigh-wave phase velocities, v_c, and quality factors, Q_R, for frequencies between 9 and 50 Hz. The Tahoma Creek drainage, located on the southwest flank of Mount Rainier, has experienced over 30 small, seasonal debris flows since 1967 (Walder and Driedger, 1995; Beason *et al.*, 2021). In recent years, several broadband seismometers have been installed along the stream channel (within 1 km) as part of an operational lahar early warning system (Kramer *et al.*, 2024). Seismic stations installed along and near the channel are a common configuration for debris flow monitoring (e.g., Arattano and Marchi, 2008; Hürlimann *et al.*, 2019; Marchi *et al.*, 2024). The station density and recurrence of events make the Tahoma Creek drainage a site of interest for modeling natural debris flows. We demonstrate how seismic properties of channel material in the drainage may affect the interpretation of high-frequency seismic energy generated by debris flows as recorded at the local stations. We compare our measured properties to a range of values typically used in similar studies in which measurements are not available (v_c between 250 and 750 m/s and Q_R between 3 and 33) by inputting the values into the theoretical debris flow seismic source model described by Farin *et al.* (2019). Overall, we find that material properties have a complex relationship with our modeled debris flow power spectral densities (PSD) and can alter the amplitude by orders of magnitude. Minor changes within the range of reasonable values may shift the frequency distribution dramatically, indicating that accurate estimates of near-surface structure are required to apply process-based models to seismic recordings of debris flows.

Methods

Hammer shot array 2022

To perform our active source experiment, we deployed ten Fairfield nodal seismometers, or nodes, perpendicular to the active channel of Tahoma Creek in an ∼90 m linear array with ∼10 m spacing for approximately four hours on 9 August 2022 (Fig. 1). The nodes are self-contained, three-component, short-period (5 Hz) seismometers that have a battery life of approximately 30 days (e.g., Farrell *et al.*, 2018, Ringler *et al.*, 2018). Although the nodes have a corner frequency of 5 Hz, they are capable of recording frequencies to below 1 Hz (Ringler *et al.*, 2018). We programmed the nodes to have a sampling rate of 500 Hz and a gain of 12 dB. Although unburied nodes are prone to high-frequency resonance (Farrell *et al.*, 2018), we were unable to bury the nodes due to permit restrictions, and instead, we identified and corrected for the resonance. We generated hammer blows adjacent to each node using a 5.4 kg sledge force hammer (PCB Piezotronics Model 086D50) with a force-plate built into the hammer head that was connected to a seismic digitizer (DATA-CUBE3) sampling at 800 Hz. Prior to and following the experiment, the force hammer was calibrated using ball drops with a known weight from a known height. In the field, we used a metal plate to provide a stable surface for the hammer blows and struck the plate ≥100 times adjacent to each node. We normalized the hammer blows to a 1 N-s impulse through the process of Allstadt *et al.* (2020), in which the hammer blows are divided by the impulse recorded from the hammer as an integral of the force–time history, then stacked to create normalized empirical Green's functions (EGFs) between each hammer location and station. Because our EGFs exhibit high power between frequencies of 9 and 50 Hz (Fig. S2, available in the supplemental material to this article), we focus on the 9–50 Hz frequency range when calculating frequency-dependent values in this study.

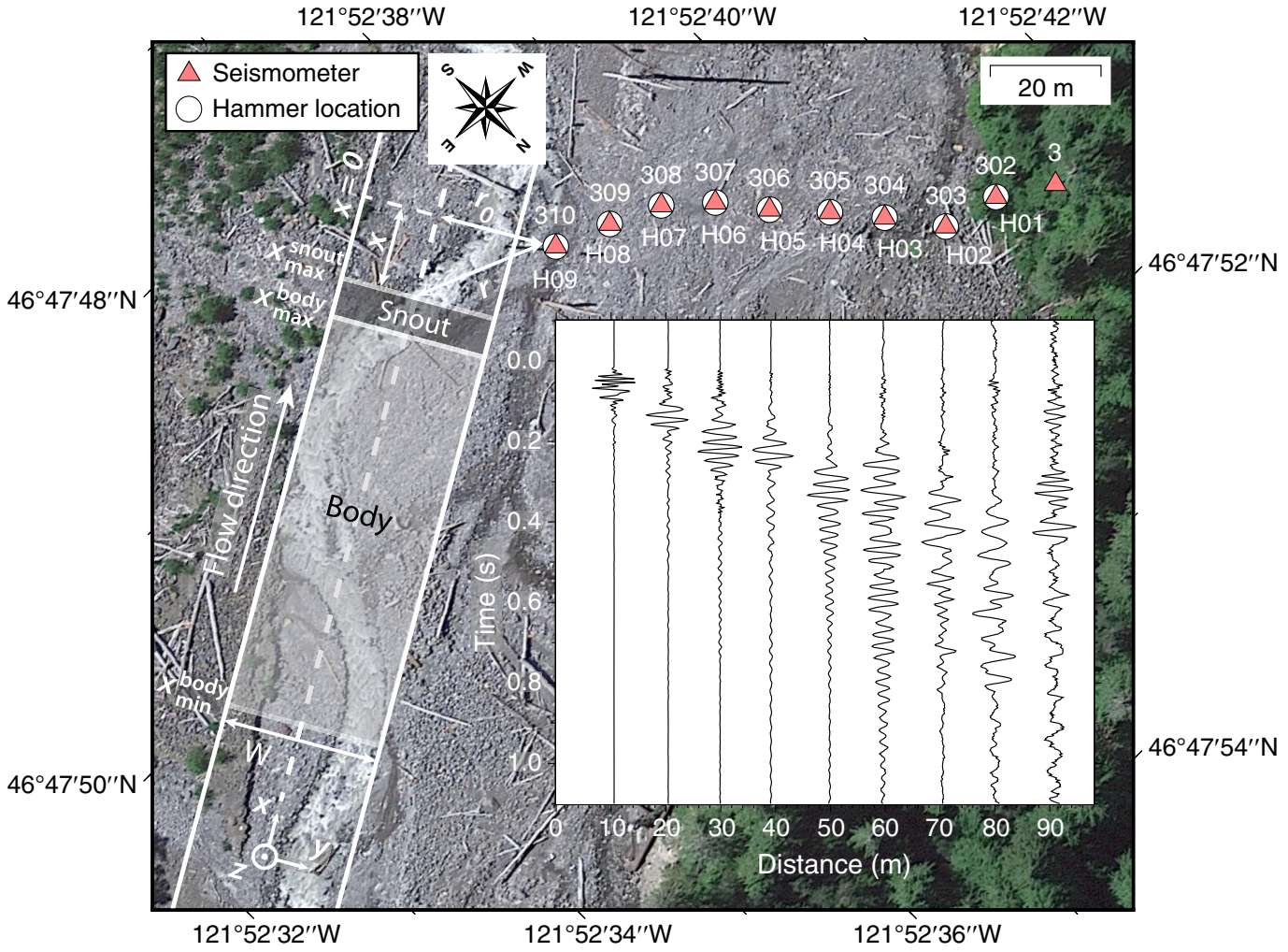

Figure 1. Map of the 9 August 2022 nodal seismometer array in Tahoma Creek, Mount Rainier, with a record section of the empirical Green's functions made from hammer blows at the location closest to the streambed, H09/310. A model schematic of a debris flow path, modified from Farin *et al.* (2019), overlays the stream. $x = 0$ corresponds to the channel location at the closest distance r_0 to the seismic station depicted in the model, here represented by station 310. Background imagery from Google (n.d.). The color version of this figure is available only in the electronic edition.

Subsurface imaging and seismic velocity calculations

Refraction. We generate a 1D *P*-wave velocity (V_P) model using our vertical-component EGFs and Refrapy, a seismic refraction Python package (Guedes *et al.*, 2022). For refraction analysis, we exclude station 3, which was not fully located in the channel, and EGFs produced from hammer location H01, which was located in a muddy depression and experienced high attenuation. For each hammer location, we assign its corresponding station as the source of the impulse (Fig. 1) and all other stations as receivers. We assume a constant spacing of 10 m between stations and assume all stations have negligible elevation change. *P*-wave arrivals were picked independently by two people (Figures S3 and S4). Travel times for these picks are inverted separately using a time-terms method (Scheidegger and Willmore, 1957; Willmore and Bancroft, 1960; Smith *et al.*, 1966) to produce two three-layer velocity models, both using a regularization weight of 10. The resulting model (Fig. 2a) is an average of the two independent time-terms models. The two velocities and average depths calculated for each layer from the time-terms models are used as error bounds. Our final depths exclude contributions from the muddy section of the channel by only including layer depths <80 m from the active channel (Figs. S3c and S4c) in the average depth calculations. We attempted but were unable to obtain a satisfactory *S*-wave velocity (V_S) model from refraction because the hammer source did not generate enough shear-wave energy.

V_P is not directly an input to the Farin *et al.* (2019) model; however, we use the V_P model derived from the refraction analysis to estimate the bulk density of the layers and corresponding error bounds using Gardner's relation (Gardner *et al.*, 1974),

$$\rho = 0.31 V_P^{0.25}, \tag{1}$$

in which ρ is the bulk density in g/cm^3 and V_P is the *P*-wave velocity in m/s.

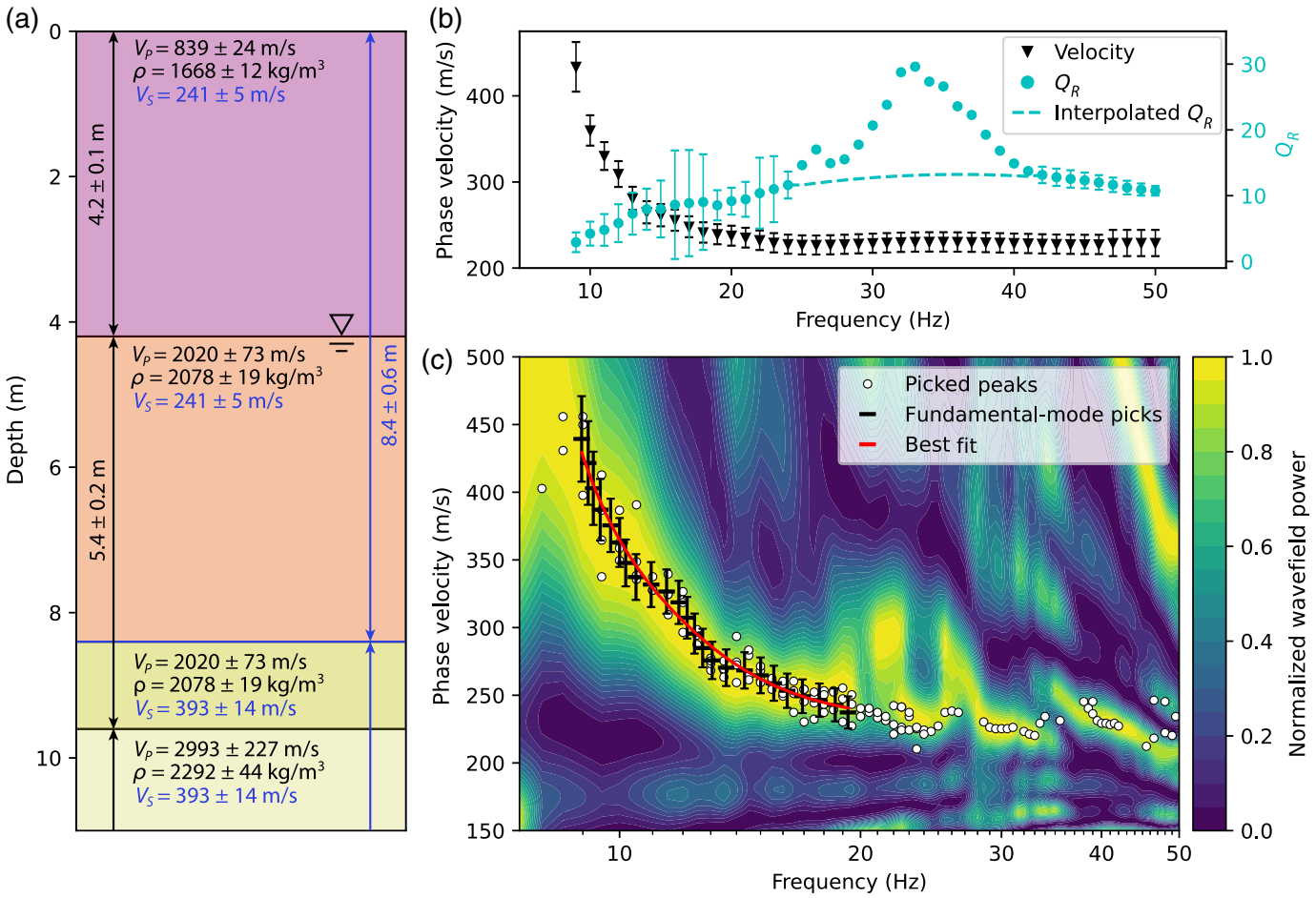

Figure 2. (a) 1D primary-wave (*P*-wave) and secondary-wave (*S*-wave) velocity profile. The *P*-wave velocity profile is identified by black text with layer thicknesses shown to the left, and the *S*-wave velocity profile has blue text and the thicknesses are shown to the right. We mark our estimate of the water table depth with an inverted triangle above two horizontal lines. (b) Phase velocity and Rayleigh-wave quality factor (Q_R) with error bars as a function of frequency in the Tahoma Creek channel. The blue-dashed line between 25 and 41 Hz marks reasonable values for Q_R in which the calculated values are assumed to be amplified. (c) Dispersion image created with empirical Green's functions between hammer location H09 and stations 309 to 305 (locations shown in Fig. 1). The color scale shows the wavefield power normalized to the maximum power at each frequency. The white circles mark picks for the fundamental mode chosen from the velocities with the greatest wavefield power on all dispersion curves used in the multichannel analysis of surface waves calculations. The black bars mark the points with standard deviation used in the dispersion curve inversion. The red line is the best-fitting dispersion curve. The color version of this figure is available only in the electronic edition.

Multichannel analysis of surface waves and inversion. We use our vertical EGFs with the multichannel analysis of surface waves (MASW) technique to estimate the 1D V_S model and directly estimate the frequency-dependent v_c. MASW is a noninvasive active-source method that uses linear seismic arrays to find surface-wave phase velocities along a transect (Park *et al.*, 1999). We invert the fundamental-mode dispersion curve to find a 1D V_S model. We use Python packages swprocess (Vantassel and Cox, 2022; Vantassel, 2024) and swprepost (Vantassel and Cox, 2020; Vantassel, 2022) to generate, prepare, and pick the dispersion curve data for the inversion. We then use the Rayleigh-wave fundamental-mode dispersion data and standard deviation as the input target for Dinver (Wathelet, 2008), an inversion framework included with the open-source software Geopsy (Wathelet *et al.*, 2020). Dinver implements the Neighborhood Algorithm to perform the inversion, which is a direct search method that uses results from previous samples to guide the following random samples (Sambridge, 1999).

We use EGFs recorded at stations 309–305 from hammer locations H09, H01, H02, and H03 for the MASW (Fig. 1) to balance the effects of the high attenuation near location H01 and incorporate as much data as possible. We estimate v_c and the associated standard deviations for the 9–50 Hz frequency band from the fundamental-mode dispersion curve but only use v_c between 9 and 20 Hz for the inversion due to the presence of higher mode surface waves and limitations from the array geometry (Fig. 2c). Our refraction-derived V_P model acts as a fixed input for Dinver, but we do not force the V_S model layer

thicknesses to match the V_P model because the inversion method is not sensitive to V_P or density (Wathelet *et al.*, 2005; Vantassel and Cox, 2020). In addition, we set the modeled V_S to increase monotonically to mitigate non-uniqueness in the inversion. For our final dispersion curve inversion, we chose to fit a four-layer velocity model and take the best-fitting curve from 50 inversions, each over 10,000 iterations. We estimate error bounds for the layer depths and velocities by calculating standard deviations from the best 100 iterations in the best-fitting inversion.

Q_R estimations

To calculate Q_R, we use a general relationship between seismic amplitude decay and distance:

$$A_i(f,r) = A_0 \frac{e^{-B(r_i - r_0)}}{\sqrt{\frac{r_i}{r_0}}}, \tag{2}$$

in which A_i is the amplitude recorded at the ith station, $B = \frac{\pi f}{Q_R v_c}$, r_i is the distance between the seismic source and ith station, r_0 is a reference length set to 1 m, A_0 is a reference amplitude, f is frequency, Q_R is the quality factor of attenuation, and v_c is phase velocity (Battaglia and Aki, 2003; Aki and Richards, 2009). Equation (2) can be linearized by taking the natural logarithm (e.g., Cannata *et al.*, 2010):

$$\ln(A_i) + 0.5 \ln\left(\frac{r_i}{r_0}\right) = \ln(A_0) - B(r_i - r_0). \tag{3}$$

We can measure A_i directly from our EGFs and r_i is known, leaving unknowns on the right side of equation (3) and allowing us to treat the equation as the slope-intercept form of a line with a slope of $-B$. We can then solve for Q_R from B.

We use the vertical EGFs between location H09 and stations 309–305 for the Q_R estimations. To isolate each frequency between 9 and 50 Hz, we filter the waveforms with a zero-phase Butterworth filter in 7 Hz bands centered on the frequency of interest. We measure A_i by taking the maximum absolute value of the filtered EGFs at the ith station. Finally, we calculate Q_R using every combination of at least three stations between 309 and 305 to find the slope, $-B$, for each combination, and then take the median values at each frequency to be the Q_R estimations. We use the interquartile range of the values at each frequency to determine uncertainty and define the error bound as half the interquartile range.

Debris flow seismic model

Farin *et al.* (2019) developed a physical model for the generation of the high-frequency (>1 Hz) seismic signals of a debris flow of constant velocity with a four-region structure flowing over a bedrock channel of constant slope. We use this model in our study because, although alternate models are available (e.g., Kean *et al.*, 2015; Lai *et al.*, 2018; Zhang *et al.*, 2021), the Farin *et al.* (2019) model is the most complete in its ability to approximate complex structures developed through the rough grain-size sorting and surging behavior that are characteristic of debris flows (Iverson, 1997; Hungr *et al.*, 2001). In addition, Arran *et al.* (2021) found this model to most accurately reproduce lab experiments of granular flows compared with other published models. In the original study, Farin *et al.* (2019) performed sensitivity tests of the modeled seismic signal to the properties of the flow using a simplified hypothetical debris flow. In this study, we expand on that investigation by using the thin-flow Farin *et al.* (2019) model with the same simplified debris flow example to investigate the sensitivity of the modeled seismic signal to the seismic properties of the channel subsurface. Although the thin-flow model matches experimental results, the flow parameters of natural debris flows change over time as the flow evolves, and we therefore expect the simplified model to less accurately predict the seismic signals produced by a natural flow. However, the model provides a framework to generally test how the path effects may alter the generated signals. We input our observed frequency-dependent attenuation and seismic velocities into the model to simulate the seismic signature of the hypothetical debris flow in Tahoma Creek. We then rerun the model with a range of v_c and Q_R values that could be reasonable for the setting, which is required when measurements are not available. Finally, we perform sensitivity tests on the influence of uncertainties in the ground properties, the average flow velocity, and the characteristic particle diameter of the modeled debris flow. We compare the results of the tests to assess the importance of accurate estimates of seismic path effects on the analysis of observed debris flows recordings.

The Farin *et al.* (2019) model estimates the power spectral density (PSD) of seismic ground velocities caused by stochastic particle impacts generating basal forces on the riverbed from the entirety of the debris flow. It models four different regions of a simplified debris flow structure that have differing particle sizes and impact rates that influence seismogenesis: (1) a saltating front of individual particles, followed by (2) the lip at the front of the main flow surge in which particles roll down and impact the channel in front of (3) the coarse-grained snout, which is the main flow front, followed by (4) the finer grained tailing body of the flow. We exclude the lip and saltating front regions in the model, as Farin *et al.* (2019) demonstrated they were trivial contributors to the seismic signal. Instead, we focus on modeling the body and the snout (Fig. 1). In addition, we assume each debris flow region has a characteristic particle diameter and the characteristic basal impulses, $\bar{I}_j$, in the radial and transverse directions are equivalent based on the final simplified PSD calculation from Farin *et al.* (2019):

$$\mathrm{PSD}_{\mathrm{tot}}(f,r_0,t) = \sum_n W R^n_{\mathrm{impact}} |2\pi f \sum_j \bar{I}_j \int_{x_{\min}(t)}^{x_{\max}(t)} \tilde{G}(f,r)_{jZ} dx|^2, \tag{4}$$

in which f is frequency, r_0 is the minimum distance between the channel and station, r is the distance between location x and the station, t is time, n identifies the debris flow region (body or snout), W is the width of the channel, j indicates the radial (R) or vertical (Z) direction, $x_{\max}(t)$ is the downslope boundary of the debris flow, and $x_{\min}(t)$ is the upslope boundary of the debris flow at time t. The rate of particle impact per unit surface area per unit particle diameter, R^n_{impact}, is defined as

$$R^n_{\text{impact}} = \frac{\tilde{u}_x \phi}{D_b D_n^2} p(D), \tag{5}$$

in which $\tilde{u}_x$ is the average velocity of the flow, ϕ is the solid particle fraction, D_n is the characteristic particle diameter of the debris flow region, D_b is the diameter of the particles causing bed roughness, and $p(D)$ is the particle diameter probability distribution in units of m^{-1}. Because of our assumption that all particles in each region of the simplified example debris flow have the same characteristic diameter, D_{snout} or D_{body}, $p(D)$ is a delta function $p(D) = \delta(D - D_n)$. The characteristic basal impulses, $\tilde{I}_j$, are defined by

$$\tilde{I}_j = (1 + e_b) m \tilde{u}_x \eta_j, \tag{6}$$

in which e_b is the coefficient of restitution of the channel bed, m is the mass of a particle defined as $m = \frac{\rho_s \pi}{6} D_n^3$, and ρ_s is the density of the material constituting the particles. η_j is a nondimensional function numerically calculated by Farin *et al.* (2019) as $\eta_R \approx 0.090\sqrt{(\delta u/\tilde{u}_x)^2/0.38 + 1}$, and $\eta_Z \approx 0.23\sqrt{(\delta u/\tilde{u}_x)^2/0.18 + 1}$, in which δu is the characteristic fluctuating speed of a particle near the bed. We assume that $\delta u \approx \tilde{u}_x$, which sets $\eta_R = 0.15$ and $\eta_Z = 0.59$. The Fourier transforms of the Green's functions in the radial and vertical directions, $\tilde{G}(f,r)_{jZ}$, are defined by

$$\tilde{G}_{jZ}(f,r) = N_{jZ} \frac{f}{4\rho_0 v_c^2(f) v_u(f)} \sqrt{\frac{v_c(f)}{fr}} e^{-\frac{\pi f r}{v_c(f) Q_R(f)}}, \tag{7}$$

in which N_{jZ} are dimensionless numbers that control the relative amplitudes of the Fourier transforms of the Green's functions in the radial (R) and vertical (Z) directions j, ρ_0 is the density of the ground, $v_c(f)$ is the phase velocity, $v_u(f)$ is the group velocity, and $Q_R(f)$ is the Rayleigh-wave quality factor. Equation (7) allows us to use our frequency-dependent ground properties to estimate the PSD caused by a hypothetical debris flow in Tahoma Creek. When we remove the frequency dependence of the ground properties while performing sensitivity tests, the velocity structure is assumed to be homogeneous. The full derivation of the simplified debris flow model can be found in Farin *et al.* (2019).

We use the same flow properties used in Farin *et al.* (2019), listed in Table 1, to model the PSD of the seismic signal of a hypothetical debris flow when it travels past a station. The seismic properties for Tahoma Creek are presented in the results section and Table S1. We estimate v_u using the close relation between v_c and v_u as described in the supplemental material. We look to the literature to provide reasonable values for Q_R and v_c in a volcanic or fluvial environment to act as inputs for our comparison models. In particular, Jolly *et al.* (2012) found bulk quality factors less than 10 on the crater walls of Whakaari/White Island, New Zealand, and lower quality factors of <5 on the unconsolidated crater floor. Petrosino *et al.* (2002) found v_c around 300 m/s above 5 Hz at Stromboli Volcano, Italy, and Piantini *et al.* (2022) found v_c equivalent

TABLE 1
Flow Parameters and Inputs Used to Model the Simplified Example Debris Flow from Farin *et al.* (2019)

Model Parameters	Inputs	Description
r_0	50 m	Distance between the closest part of the channel and the receiver
l_b	1000 m	Length of body
l_s	100 m	Length of snout
W	10 m	Width of the flow
D_{body}	0.25 m	Particle diameter in the body
D_{snout}	0.5 m	Particle diameter in the snout
D_{bed}	0.25 m/ 0.5 m	Diameter of particles forming bed roughness (assumed to be the same as particle diameter)
H	1 m	Thickness of the flow
$\tilde{u}_x$	10 m/s	Average velocity of the flow
Θ	10°	Slope of channel
ϕ	0.6	Solid particle fraction
e_b	0.5	Coefficient of restitution
ρ_s	2500 kg/m^3	Density of material constituting the particles
N_{ZZ}	0.6	Coefficient in Green's function linked to z direction*
N_{RZ}	0.8	Coefficient in Green's function linked to radial direction*
η_Z	0.59	Basal impact coefficient linked to z direction†
η_R	0.15	Basal impact coefficient linked to radial direction†
ρ_0	1700 kg/m^3	Density of ground‡

*Typical values reported in Gimbert *et al.* (2014).
†Numerically calculated in Farin *et al.* (2019).
‡Average rock bulk density of ash-dominated material at Mount Rainier in Totman *et al.* (2014).

to 200 m/s fit data between 5 and 20 Hz recorded from a braided river in the French Alps. Lai *et al.* (2018), which analyzes seismic properties of a debris flow in Montecito, California, uses values of 953 ± 200 m/s for v_c and 45 ± 15 for the quality factor. These studies guide the low and high bounds for v_c, 250–750 m/s, and Q_R, 3–33, used as inputs to the Farin *et al.* (2019) debris flow model for comparison against our measured subsurface properties. v_u is estimated to be equivalent to $v_c/1.48$. To perform sensitivity tests of the flow properties, we vary the average flow velocity, $\bar{u}_x$, between typical debris flow velocities of 5–40 m/s (Allstadt *et al.*, 2018) and vary the characteristic particle diameter, D, between 0.001 and 1.2 m, following the sensitivity tests performed by Farin *et al.* (2019) and typical debris flow particle diameters (Hungr *et al.*, 2001).

Results

1D velocity structure

Our *P*- and *S*-wave velocity models indicate there are two distinct V_P changes and one V_S change in the upper 11 m of the Tahoma Creek channel transect (Fig. 2a). We find that the upper 4.2 ± 0.1 m defines a layer with a V_P of 839 ± 24 m/s. We estimate the density of the layer to be approximately 1668 ± 12 kg/m^3 through the use of Gardner's relation (equation 1; Gardner *et al.*, 1974). Our density estimation is consistent with an average rock bulk density of 1700 kg/m^3 calculated for ash-dominated near-surface material at Mount Rainier (Totman *et al.*, 2014) and estimates of 1500–1800 kg/m^3 for the bulk density of river sediment from the volcano (Czuba *et al.*, 2012). V_P increases to 2020 ± 73 m/s at the layer boundary, but V_S does not change. We interpret the V_P change to be the presence of the water table because the water table may cause a jump in V_P to above the speed of sound in water (~1500 m/s) and would not have a similar effect on the V_S model. The 2020 ± 73 m/s V_P layer has a thickness of 5.4 ± 0.2 m and an estimated density of 2078 ± 19 kg/m^3. Below the second layer, V_P increases to 2993 ± 227 m/s, producing a density estimate of 2292 ± 44 kg/m^3. We are uncertain about the thickness of the third layer because we lose resolution with the refraction analysis at depths >10 m. The V_S profile consists of two layers within our resolution limits, an upper 8.4 ± 0.6-m-thick layer with a velocity of 241 ± 5 m/s and a lower layer with a velocity of 393 ± 14 m/s. We lose resolution with the dispersion curve inversion around a depth of 17 m before the second V_S change.

Phase velocity and Q_R

In the Tahoma Creek channel, we find that v_c is approximately 434 m/s at 9 Hz, sharply decreases to ~230 m/s by 23 Hz, and remains fairly steady at ~230 m/s up to 50 Hz (Fig. 2b). Q_R is relatively steady between 7 and 14 except for frequency bands 9 to 13 Hz, in which the values increase from the minimum Q_R of 2.9 to 7.3, and 25 to 41 Hz, in which the values peak at 29.6 (Fig. 2b). We find the largest spread in Q_R produced from resampling between 30 and 37 Hz, with the greatest interquartile range reaching 27.5 at 31 Hz, indicating significant uncertainty (Fig. S7). We interpret the high Q_R values between 25 and 41 Hz to be from resonance of the nodes, rather than a quality of the channel properties. The instruments may oscillate at high frequencies due to the location of the geophone in the top of the node, which is known to result in resonance and amplify the signals. Similar instrumental amplification was documented by Farrell *et al.* (2018). Because we were unable to bury the nodes at this site, we therefore correct for the oscillation-caused amplification between 25 and 41 Hz by interpolating Q_R from a second-degree polynomial fit to the surrounding frequencies (Fig. S8). The interpolated Q_R values are between 11.9 and 13.3 (Fig. 2b). Calculated values and error bounds for v_c and Q_R are reported in Table S1.

Analytic debris flow model

We input our measured v_c and Q_R into the simplified debris flow model adapted from Farin *et al.* (2019) and compare the results with PSDs modeled using our range of test seismic properties, 3–33 for Q_R and 250–750 m/s for v_c. The frequency-dependent observed seismic properties generally produce a bimodal PSD with a relatively narrower, low-frequency peak between ~9 and 19 Hz and a wider, high-frequency peak between ~19 and 50 Hz (Fig. 3a). The low-frequency peak is more prominent than the high-frequency peak when the hypothetical debris flow is far from the station (in which $x < -500$ m in Fig. 3c). While the modeled debris flow approaches and passes the station, the high-frequency energy grows relative to the low-frequency energy, but the bimodal PSD distribution persists. Setting Q_R, v_c, and v_u to constant values produces a single peak in the PSD distribution (Fig. 4).

By investigating values between 3 and 33 for Q_R and 250 and 750 m/s for v_c, we explore the effects of varying seismic properties on the modeled PSDs (Fig. 4). When v_c is constant, larger values of Q_R result in more high-frequency energy reaching the station, which causes an increase in frequency in which the PSD peak occurs (Fig. 4b). For example, increasing Q_R from 27 to 33 increases the frequency of the peak by a factor of ~1.2 for all velocities, and changing Q_R from 3 to 9 increases the frequency by a factor of ~3 (Table 2). Reducing attenuation by increasing Q_R results in substantial increases in PSD, though the changes in power from adjustments to Q_R are more prominent when attenuation is high. For example, increasing Q_R from 27 to 33 results in an approximately 1.8 factor increase in the maximum PSD, and increasing Q_R from 3 to 9 increases the maximum PSD by a factor of ~27.0 (Table 3). Increasing v_c results in lower PSD values and shifts the peaks to higher frequencies (Fig. 4a). When Q_R is constant, the maximum PSD decreases by a factor of ~1.96 when increasing v_c from 250 to 350 m/s and decreases by a factor of ~1.33 when increasing the velocity from 650 to 750 m/s (Table 3). Although the frequency at which the PSD peak occurs always

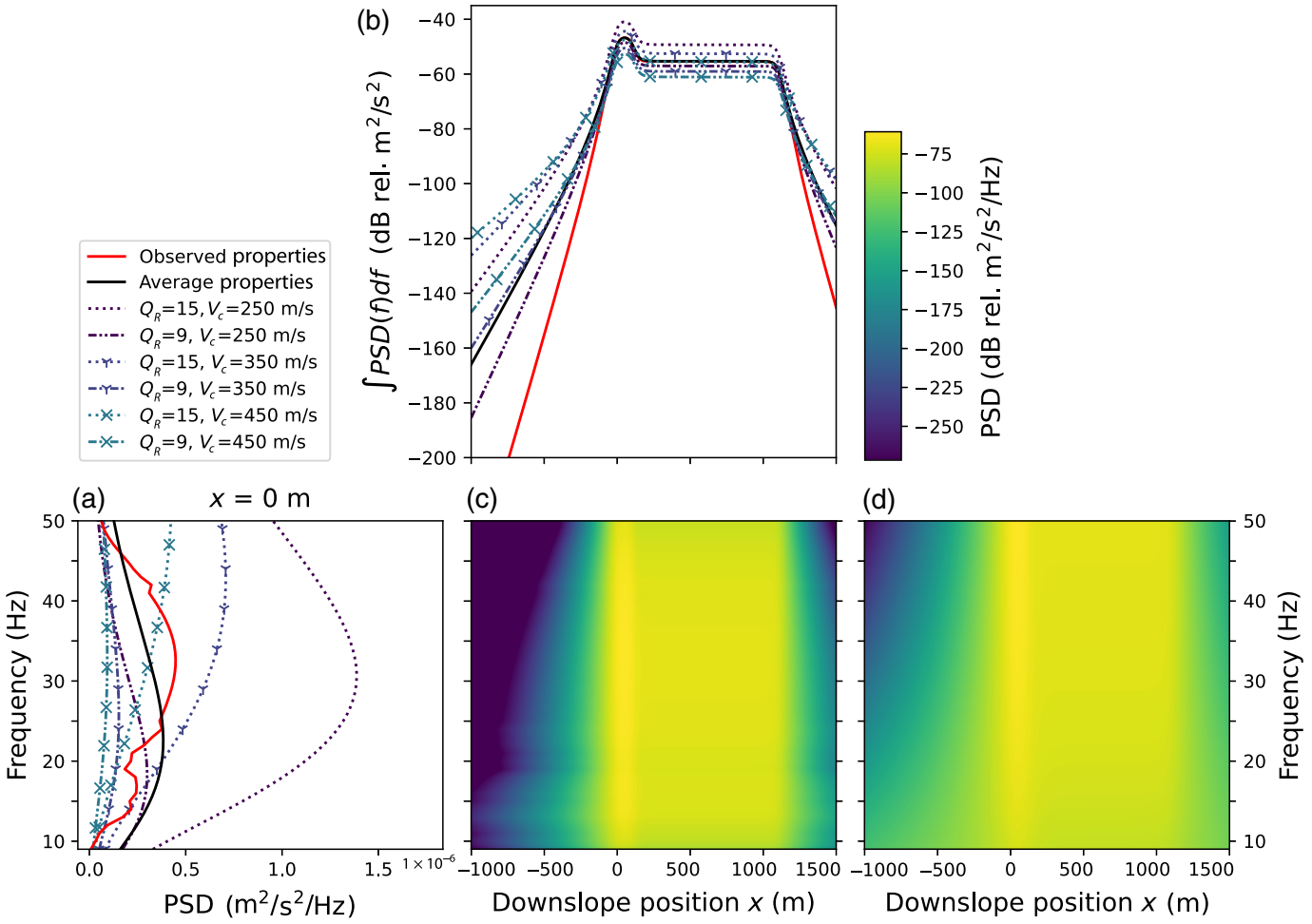

Figure 3. Plots comparing the power spectral density (PSD) modeled with observed values for the Rayleigh-wave quality factor, Q_R, and phase velocity, v_c, to modeled PSDs using hypothetical values for Q_R and v_c. (a) Modeled PSDs varying v_c in 100 m/s intervals between 250 and 450 m/s and varying Q_R between 9 and 15. The PSD modeled from observed seismic properties (red line) is plotted against the other PSDs. The PSDs are modeled at position x = 0 m, in which x corresponds to the distance between the downslope boundary of the snout and the closest part of the channel to the receiver. (b) PSDs of each modeled flow in panel (a) integrated over all frequencies f = 9–50 Hz as a function of x. (c) Spectrogram of the PSD of the modeled debris flow with observed, frequency-dependent values for Q_R and v_c in the Tahoma Creek channel. (d) Spectrogram of the PSD of the modeled debris flow with v_c = 450 m/s and Q_R = 15. The color bar provides the values for both (c) and (d). The color version of this figure is available only in the electronic edition.

increases with increasing v_c, the extent of the change in frequency is dependent on Q_R. For example, when Q_R is 33, the frequency of the PSD peak changes by ~27 Hz with a velocity increase of 100 m/s (Table 2). Alternatively, when Q_R is 3, the frequency of the peak only increases by ~2.4 Hz for the same velocity change (Table 2). Overall, the width of the PSD curve extends over a broader frequency range with increasing v_c or increasing Q_R.

When we integrate the PSDs over the length of the debris flow and frequency (equations S2 and S3), we find that Q_R ranging from 3 to 33 produces values between 1.85×10^{-6} m^2/s^2 and 2.38×10^{-2} m^2/s^2 for a frequency range of 0–300 Hz when $\bar{u}_x$ is 22 m/s and the particle diameter is 0.6 m. When we hold Q_R constant at 18 and vary v_c from 250 to 750 m/s, the integrated PSDs are between 1.52×10^{-3} m^2/s^2 and 4.80×10^{-3} m^2/s^2 with the same frequency band and flow properties (Fig. 5a). Because of the frequency dependence of the channel properties, a narrower frequency band of 9–50 Hz produces integrated PSDs between 1.50×10^{-6}m^2/s^2 and 8.71×10^{-4}m^2/s^2 for the same Q_R range and between 9.01×10^{-5} m^2/s^2 and 2.65×10^{-3} m^2/s^2 for the same v_c range (Fig. 5b). When we compare the influence of channel properties with the integrated PSDs made by varying average flow velocity between 5 and 40 m/s and varying particle diameter between 0.001–1.2 m, we find that the average debris flow velocity has a similar influence as Q_R, with the integrated PSD ranging over roughly two orders of magnitude from 2.81×10^{-5} m^2/s^2 to 1.44×10^{-2} m^2/s^2 within the 0–300 Hz frequency band and 4.40×10^{-6} m^2/s^2 to 2.25×10^{-3} m^2/s^2 within the 9–50 Hz band (Fig. 5). Our test particle diameters cover a wide range of possible clast sizes, strongly influencing the modeled power

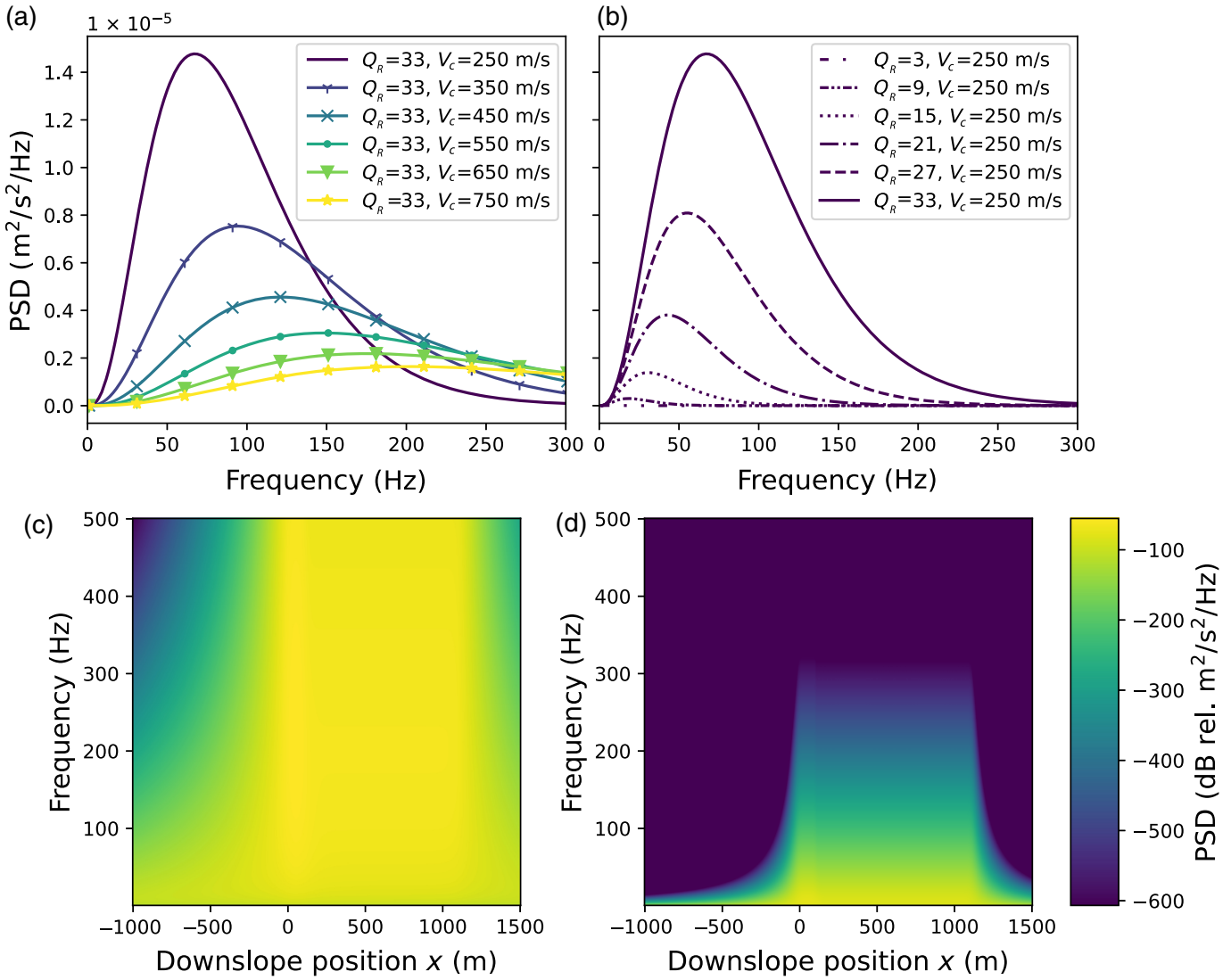

generated by the flow, with the integrated PSD ranging from 1.11×10^{-11} m^2/s^2 to 1.91×10^{-2} m^2/s^2 within the 0–300 Hz frequency band and 1.74×10^{-12} m^2/s^2 to 3.00×10^{-3} m^2/s^2 within the 9–50 Hz band (Fig. 5).

In general, the PSDs are greatest when the modeled debris flow is at x = 50 m, corresponding to the point at which the upstream and downstream boundaries of the snout are equidistant to the receiver. The PSDs integrated over all frequencies at positions x = −500 to 1500 m have similar shapes for both the observed and test seismic properties, with the exception that the total PSD from the observed seismic properties increases more rapidly approaching x = ∼0 m and decreases more rapidly at distances of x > ∼1100 m than the PSDs produced with the test seismic properties (Fig. 3b). As the debris flow approaches x = 50 m, the frequency at which the peak PSD value occurs generally increases and a wider frequency band is excited. For example, Q_R = 33 and v_c = 250 m/s produce a maximum PSD peak at 71 Hz when x = 50 m (Fig. 4c). Because the snout moves downstream from the receiver, the lower-energy body starts to dominate the signal and the PSD decreases as a result.

Figure 4. Plots comparing the power spectral density (PSD) modeled with different values for the Rayleigh-wave quality factor, Q_R, and phase velocity, v_c. (a) Modeled PSDs varying v_c in 100 m/s intervals between 250 and 750 m/s with Q_R = 33. The PSDs are modeled at x = 0 m, in which x corresponds to the distance between the downslope boundary of the snout and the closest part of the channel to the receiver. (b) Modeled PSDs varying Q_R in intervals of 6 between 3 and 33 with v_c = 250 m/s. The PSDs are modeled at x = 0 m. The solid purple line corresponding to the PSD modeled with Q_R = 33 and v_c = 250 m/s is plotted in both (a) and (b). (c) Spectrogram of the total PSD amplitude of the modeled debris flow with v_c = 750 m/s and Q_R = 33. (d) Spectrogram of the total PSD amplitude of the modeled debris flow with v_c = 250 m/s and Q_R = 3. The color bar provides the values for both (c) and (d). The color version of this figure is available only in the electronic edition.

When the body fully dominates the signal, the PSD peak occurs at 67 Hz, a slightly lower frequency than the snout. For a full discussion on how the PSD is affected by each modeled debris flow section, refer to Farin *et al.* (2019).

TABLE 2
Frequency at Which the Maximum Modeled Power Spectral Density (PSD) Values Occur Based on Input Quality Factor, Q_R, and Phase Velocity, v_c

	Q_R					
v_c	**3**	**9**	**15**	**21**	**27**	**33**
250 m/s	6 Hz	18 Hz	31 Hz	43 Hz	55 Hz	67 Hz
350 m/s	9 Hz	26 Hz	43 Hz	60 Hz	77 Hz	94 Hz
450 m/s	11 Hz	33 Hz	55 Hz	77 Hz	99 Hz	121 Hz
550 m/s	13 Hz	40 Hz	67 Hz	94 Hz	121 Hz	148 Hz
650 m/s	16 Hz	48 Hz	80 Hz	111 Hz	143 Hz	175 Hz
750 m/s	18 Hz	55 Hz	92 Hz	129 Hz	165 Hz	202 Hz

The PSD is generated using the thin-flow model described in Farin *et al.* (2019) and the hypothetical debris flow parameters provided in Table 1 for position x = 0 m.

Discussion

Our study area in the Tahoma Creek stream channel demonstrates seismic properties consistent with the drainage's history of fluvial and debris flow activity. We find low-*P*- and *S*-wave velocities of 840 ± 25 m/s and 241 ± 5 m/s, respectively, in the near surface in which the channel consists of unconsolidated deposits ranging from fine sand to boulders deposited by past debris flows. Based on our *P*- and *S*-wave velocity profiles, we interpret that the deposits extend to a depth of at least 11 m and that bedrock is below our resolution depth (Fig. 2a). Although it is likely that there are thin lenses of material and substantial intricacies even within our study area, we are instead focused on finding more general seismic properties that may be applied to a wider section of the Tahoma Creek stream channel to assist with analysis of the seismic data from debris flows within the drainage. In particular, the recordings from the broadband seismometers recently installed adjacent to the stream (Kramer *et al.*, 2024) will be strongly influenced by the near-surface channel properties. Our findings allow us to consider an approximate path contribution from the channel rather than relying solely on the material properties of the surrounding, more consolidated hillslopes when interpreting or modeling debris flow seismic signals in the Tahoma Creek drainage.

We find that v_c and Q_R range between 226–434 m/s and 2.9–13.3, respectively, for frequencies between 9 and 50 Hz. The values are low, but not atypical for unconsolidated volcanic or alluvial deposits such as the material found in the Tahoma Creek stream channel (e.g., Petrosino *et al.*, 2002; Jolly *et al.*, 2012; Piantini *et al.*, 2022). An important aspect of using our empirical seismic properties to model the seismic signature of a hypothetical debris flow is that we are able to investigate the effect of the frequency dependence of v_c, v_u, and Q_R on the modeled PSDs. The bimodal PSD produced with the observed seismic properties is a result of the frequency

TABLE 3
Maximum Modeled Power Spectral Density (PSD) Values Based on Input Quality Factor, Q_R, and Phase Velocity, v_c

	Q_R					
v_c	**3**	**9**	**15**	**21**	**27**	**33**
250 m/s	1.109×10^{-8} $m^2/s^2/Hz$	2.995×10^{-7} $m^2/s^2/Hz$	1.387×10^{-6} $m^2/s^2/Hz$	3.807×10^{-6} $m^2/s^2/Hz$	8.092×10^{-6} $m^2/s^2/Hz$	1.477×10^{-5} $m^2/s^2/Hz$
350 m/s	5.645×10^{-9} $m^2/s^2/Hz$	1.529×10^{-7} $m^2/s^2/Hz$	7.079×10^{-7} $m^2/s^2/Hz$	1.942×10^{-6} $m^2/s^2/Hz$	4.128×10^{-6} $m^2/s^2/Hz$	7.538×10^{-6} $m^2/s^2/Hz$
450 m/s	3.426×10^{-9} $m^2/s^2/Hz$	9.250×10^{-8} $m^2/s^2/Hz$	4.282×10^{-7} $m^2/s^2/Hz$	1.175×10^{-6} $m^2/s^2/Hz$	2.497×10^{-6} $m^2/s^2/Hz$	4.560×10^{-6} $m^2/s^2/Hz$
550 m/s	2.289×10^{-9} $m^2/s^2/Hz$	6.191×10^{-8} $m^2/s^2/Hz$	2.867×10^{-7} $m^2/s^2/Hz$	7.866×10^{-7} $m^2/s^2/Hz$	1.672×10^{-6} $m^2/s^2/Hz$	3.052×10^{-6} $m^2/s^2/Hz$
650 m/s	1.642×10^{-9} $m^2/s^2/Hz$	4.433×10^{-8} $m^2/s^2/Hz$	2.052×10^{-7} $m^2/s^2/Hz$	5.632×10^{-7} $m^2/s^2/Hz$	1.197×10^{-6} $m^2/s^2/Hz$	2.185×10^{-6} $m^2/s^2/Hz$
750 m/s	1.233×10^{-9} $m^2/s^2/Hz$	3.330×10^{-8} $m^2/s^2/Hz$	1.542×10^{-7} $m^2/s^2/Hz$	4.230×10^{-7} $m^2/s^2/Hz$	8.991×10^{-7} $m^2/s^2/Hz$	1.642×10^{-6} $m^2/s^2/Hz$

The PSD is generated using the thin-flow model described in Farin *et al.* (2019) and the hypothetical debris flow parameters provided in Table 1 for position x = 0 m.

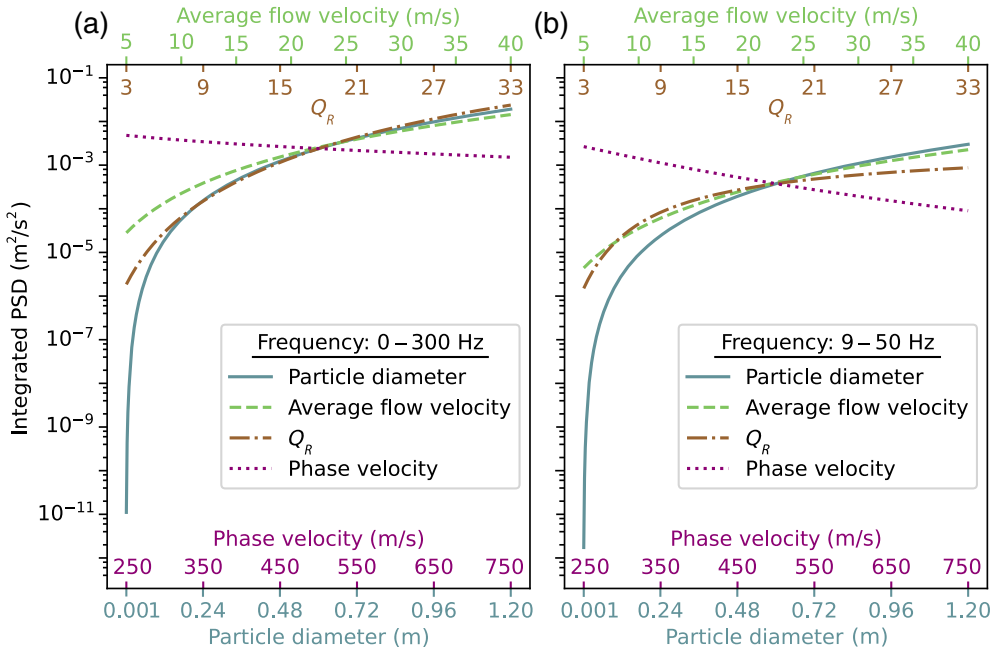

Figure 5. Modeled power spectral density (PSD) curves of a hypothetical debris flow integrated over frequency bands of (a) 0–300 Hz and (b) 9–50 Hz. Each line depicts the integrated PSD made by varying the parameter provided in the legend. When held constant for the hypothetical flow, the Rayleigh-wave quality factor (Q_R) is 18, the phase velocity is 500 m/s, the average velocity of the flow is 22 m/s, and the characteristic particle diameter is 0.6 m. The color version of this figure is available only in the electronic edition.

dependence because the PSDs produced with the constant test values are unimodal (Figs. 3a and 4). The low-frequency peak we observe in the bimodal distribution is greatly influenced by the attenuation component of the Green's function. The phase velocity is relatively high (~434–230 m/s) between ~9 and 19 Hz (Fig. 2b), causing relatively low attenuation despite low Q_R in this frequency range.

At frequencies above 19 Hz, the observed v_c and Q_R stabilize at around 230 m/s and between 10 and 13, respectively (Fig. 2b), creating the higher frequency peak in the PSD that visually behaves similarly to the frequency-independent PSD curves. In particular, the high-frequency energy modeled to reach the station rapidly increases when the debris flow approaches the instrument, reaching the greatest values when x = 50 m and the high-frequency peak in the bimodal PSD becomes more prominent than the low-frequency peak (Figs. 3 and 4).

The high-frequency peak modeled from the observed, frequency-dependent seismic properties does not exactly match the modeled PSDs made with constant seismic properties even when the PSDs are created with constant properties that approximately match the stable values above ~19 Hz (Fig. 3a). Specifically, neither the peak PSD values nor the frequencies at which the peaks occur match between the PSD with observed seismic properties and the PSD made with an average of the observed properties (v_c = 230 m/s, v_u = 230 m/s, and Q_R = 12; Fig. 3a). However, the PSD from observed properties integrated over all frequencies as a function of x matches both the integrated PSD made with the average observed properties and the integrated PSD from a v_c of 450 m/s and Q_R of 15 when x is between 0 and 1100 m (Fig. 3b), despite differing in frequency content. For example, at position x = 0 m, the peak value of the PSD generated with the observed properties occurs at a frequency of 33 Hz, but the PSD generated with a v_c of 450 m/s and Q_R of 15 occurs at a frequency above the 50 Hz maximum of our observed properties. Because many seismic sensors have sampling rates at or below 100 Hz (e.g., Havskov and Alguacil, 2016; Davis, 2024), our results indicate that the non-uniqueness in the frequency-limited integrated PSDs could be important for real-world analysis. At x values less than 0 m or greater than 1100 m (i.e., as the flow approaches and retreats), the integrated PSD made with the observed properties is substantially lower than the integrated PSD from a v_c of 450 m/s and Q_R of 15, or from the average observed properties. As a result, automated seismic detectors may require a debris flow to be closer to a station to recognize an increase in seismic energy corresponding to the event if the frequency dependence of the material properties is not considered. In addition, methods that rely on seismic amplitude or power to estimate source–station distance may require site-specific calibrations. Despite relatively stable values for v_c and Q_R above ~19 Hz, the frequency dependence still greatly influences the PSD results.

Our modeling results using v_c between 250 and 750 m/s and Q_R between 3 and 33 demonstrate the importance of having accurate near-surface seismic properties when interpreting the signals generated by debris flows. The seismic material properties influence the power of the waveforms and the frequencies that are recorded in complex ways. As expected, high attenuation greatly diminishes the modeled PSDs and restricts the high-power waves to low frequencies (Fig. 4b). However, increasing v_c reduces the power of the generated waves (Fig. 4a), which could counteract the increase in power from low attenuation or amplify the effect of high attenuation. The

difficulty in separating the seismic signal from uncertain path effects when interpreting debris flow seismic waves is further exacerbated by the nature of a debris flow as an elongated moving source. We often do not know the exact location of a debris flow as it occurs, which creates an additional variable when attempting to link physical properties of the flow to the power or frequency content of the recorded waves. Our model results indicate that the power estimate for a flow could be off by an order of magnitude if v_c is assumed to be 750 m/s and the true value is 250 m/s. Even assuming Q_R is 21 when the true value is 3 results in power estimates that are off by two orders of magnitude (Fig. 4).

Our findings for seismic ground properties are unique to the Tahoma Creek channel, but can inform expected values in other channels at Mount Rainier and similar settings. For many studies on the seismic signals generated by debris flows, path effects may represent large sources of uncertainty or error (e.g., Allstadt *et al.*, 2019, 2020; Marchi *et al.*, 2024), and important smaller features like stream channels are often below the resolution of studies focused on regional seismic ground properties. Our results provide evidence that studies focused on debris flow seismic signals may need to consider higher attenuation and lower velocity values than would generally be identified for the surrounding region. Ideally, detailed Green's functions would be generated for any study location focused on surface processes, though many areas are too remote or dangerous to perform active source experiments similar to the one performed for this study. The seismic properties we found for the Tahoma Creek channel are consistent with the relatively limited dataset of other studies that quantify values for similar features in near-surface environments (e.g., Petrosino *et al.*, 2002; Jolly *et al.*, 2012; Piantini *et al.*, 2022), and may be used in other locations to influence decisions for initial estimates of seismic ground properties. Site-specific calibrations may be required, however, because our results indicate errors in seismic ground properties may cause great uncertainty when interpreting debris flow seismic signals, particularly for errors in Q_R when attenuation is high (i.e., $Q_R < 10$; Fig. 5).

Although our analysis primarily focuses on a hypothetical debris flow modeled with the parameters listed in Table 1, the classification of a debris flow encompasses a wide range of flow parameters. Debris flows may contain clasts ranging from clay to boulders (Hungr *et al.*, 2001), and the seismic energy generated by the flow is greatly dependent on the clast size (Tsai *et al.*, 2012). Our results indicate that particle diameters ranging from 0.001 to 1.2 m produce PSDs that differ by approximately nine orders of magnitude (Fig. 5), further emphasizing the influence that particle size has on seismic power. The power modeled for the flow most appreciably changes when particle diameters range between 0.001 and 0.1 m, with this subset of values accounting for ~6 orders of magnitude change in our modeled PSDs (Fig. 5). In addition, most debris flows can reach flow velocities up to 10 m/s, but may travel slower or faster depending on channel conditions and overall flow properties (Hungr *et al.*, 2001). We find that a range of flow velocities from 5 to 40 m/s can influence the PSD of the seismic signal by up to two orders of magnitude (Fig. 5).

Despite the clear dependence of the generated seismic signals on the flow properties, the ground properties also strongly influence the signals recorded from the events. Particularly, high attenuation in the channels through which the flows travel, modeled with Q_R values ranging from 3 to 33, produce PSDs that differ by approximately four orders of magnitude when considering a frequency band up to 300 Hz (Fig. 5a). Although a large error in the particle diameter has the potential to alter the modeled seismic power from a debris flow by ~9 orders of magnitude, the largest change in power is associated with errors when particle diameters are <0.1 m (Fig. 5). The smallest particle diameters also generate the least amount of power out of all model parameters tested in this study (Fig. 5), which implies small debris flows with primarily fine grains may not often be observable above noise level on seismometers offset from the channel. Effective particle diameters >0.1 m therefore represent more practical values for debris flows that may be detected by seismometers used for debris flow monitoring, and our tests indicate that input particle diameters ranging between 0.1 and 1.2 m have approximately the same influence on generated seismic power as the attenuation and average flow velocity in our model (Fig. 5). Our results indicate that errors in both ground and flow properties may greatly affect modeled debris flow seismic power. While the theory behind the generation of seismic signals from debris flows is being developed, eliminating any error source can help progress our understanding and allow models to more accurately reproduce debris flow seismic signals.

The frequency dependence of Q_R is important to note. Because attenuation has a greater influence on higher frequencies (Shearer, 2009), the influence of Q_R decreases when the frequency band is limited to <50 Hz (Fig. 5b). As previously mentioned, many seismic monitoring stations have sampling rates less than 100 Hz. The influence of Q_R could therefore be less substantial in many real-world applications than in the results presented here. However, most debris flows are relatively small and primarily generate high-frequency energy >1 Hz, and along-channel seismometers may record signals up to hundreds of samples per second (e.g., Allstadt *et al.*, 2018). Progress on understanding how the high-frequency energy generated by debris flows relates to flow properties is reliant on how well we can interpret recorded seismic signals. Accurately correcting for the path effects can enable more accurate interpretations.

Conclusion

The seismic waves recorded from debris flows are often complicated to interpret. In recent years, several authors have proposed analytic and numerical modeling strategies for debris

flows in an effort to relate recorded seismic signals to properties of the flows. However, the seismic properties of the stream channels through which the debris flows travel are often unknown or poorly constrained and can greatly influence the results of the models, including the frequency content and amplitude of the waves. We performed an active source experiment to estimate 1D *P*- and *S*-wave velocity profiles, v_c, and Q_R for frequencies between 9 and 50 Hz in the Tahoma Creek drainage at Mount Rainier, Washington, then performed tests on the effects of ground properties on the seismic energy modeled from a debris flow. Our results indicate that the channel materials are highly attenuative and frequency dependent, which greatly reduces the power recorded from an event at increasing distances and may result in delayed detection when events occur. The ground properties have a complex relationship with the modeled seismic signals, but generally, higher attenuation decreases the total power recorded from an event and shifts the highest power to lower frequencies. Greater phase velocities will also reduce the total power, but simultaneously shift the highest power to lower frequencies. We find that the effective particle diameter as used in the model developed by Farin *et al.* (2019) has a very strong influence on the modeled debris flow seismic power, with the modeled PSDs differing by approximately nine orders of magnitude when the input particles range in size from clay to boulders. Our values for the ground properties do not influence the model as greatly as particle diameter, but are shown to vary the modeled PSD by up to four orders of magnitude, which is comparable with the range in power generated by the average flow velocity and the particle diameters most likely to generate enough power to be observable on seismic instruments. High-quality estimates for seismic channel properties can be beneficial to progress efforts to model debris flow seismic signals to better monitor and understand future events.

Data and Resources

The nodal seismometer and force hammer data are available on Zenodo (Conner *et al.*, 2025). The supplemental material contains refraction results, dispersion curve inversion results, the frequency-dependent Rayleigh-wave group velocity calculation from the phase velocities, quality factor amplification corrections, analysis of error on the frequency-dependent ground properties, and a list of the frequency-dependent channel properties calculated for the Tahoma Creek stream channel between 9 and 50 Hz.

Declaration of Competing Interests

The authors acknowledge that there are no conflicts of interest recorded.

Acknowledgments

The authors would like to thank Alicia Hotovec-Ellis and one anonymous reviewer for their constructive comments. The authors would also like to thank and acknowledge all volunteers who assisted with nodal seismometer deployments in the Tahoma Creek stream channel. In particular, the authors would like to thank Amberlee Darold and D. J. Miller for assisting with the active source experiment. Figure 1 was partially created using the Generic Mapping Tools (GMT) software (Wessel *et al.*, 2013). The research is funded by the U.S. Geological Survey (Cooperative Agreement, CFDA Number 15.818).

Any use of trade, firm, or product names is for descriptive purposes only and does not imply endorsement by the U.S. Government.

References

Aki, K., and P. G. Richards (2009). *Quantitative Seismology*, University Science Books, Mill Valley, California New York.

Allstadt, K. E., M. Farin, R. M. Iverson, M. K. Obryk, J. W. Kean, V. C. Tsai, T. D. Rapstine, and M. Logan (2020). Measuring Basal force fluctuations of debris flows using seismic recordings and empirical Green's functions, *J. Geophys. Res. Earth Surf.* **125,** no. 9, e2020JF005590, doi: 10.1029/2020JF005590.

Allstadt, K. E., M. Farin, A. B. Lockhart, S. K. McBride, J. W. Kean, R. M. Iverson, M. Logan, J. B. Smith, V. C. Tsai, and D. George (2019). Overcoming barriers to progress in seismic monitoring and characterization of debris flows and lahars, Mountain Scholar, doi: 10.25676/11124/173234.

Allstadt, K. E., R. S. Matoza, A. B. Lockhart, S. C. Moran, J. Caplan-Auerbach, M. M. Haney, W. A. Thelen, and S. D. Malone (2018). Seismic and acoustic signatures of surficial mass movements at volcanoes, *J. Volcanol. Geotherm. Res.* **364,** 76–106, doi: 10.1016/j.jvolgeores.2018.09.007.

Arattano, M., and L. Marchi (2008). Systems and sensors for debris-flow monitoring and warning, *Sensors* **8,** no. 4, 2436–2452, doi: 10.3390/s8042436.

Arran, M. I., A. Mangeney, J. De Rosny, M. Farin, R. Toussaint, and O. Roche (2021). Laboratory Landquakes: Insights from experiments into the high-frequency seismic signal generated by geophysical granular flows, *J. Geophys. Res. Earth Surf.* **126,** no. 5, e2021JF006172, doi: 10.1029/2021JF006172.

Battaglia, J., and K. Aki (2003). Location of seismic events and eruptive fissures on the Piton de la Fournaise volcano using seismic amplitudes, *J. Geophys. Res.* **108,** no. B8, 2002JB002193, doi: 10.1029/2002JB002193.

Beason, S. R., N. T. Legg, T. R. Kenyon, and R. P. Jost (2021). Forecasting and seismic detection of Proglacial debris flows at Mount Rainier National Park, Washington, USA, *Environ. Eng. Geosci.* **27,** no. 1, 57–72, doi: 10.2113/EEG-D-20-00014.

Cannata, A., G. Di Grazia, P. Montalto, F. Ferrari, G. Nunnari, D. Patanè, and E. Privitera (2010). New insights into banded tremor from the 2008–2009 Mount Etna eruption, *J. Geophys. Res.* **115,** no. B12, 2009JB007120, doi: 10.1029/2009JB007120.

Conner, A., A. Thomas, W. Thelen, K. Allstadt, A. Iezzi, and E. Collins (2025). 9 August 2022 nodal seismometer Hammer array data, Tahoma Creek, Mount Rainier, *Zenodo*, doi: 10.5281/zenodo.14903076.

Czuba, J. A., C. S. Magirl, C. R. Czuba, C. A. Curran, K. H. Johnson, T. D. Olsen, H. K. Kimball, and C. C. Gish (2012). Geomorphic analysis of the river response to sedimentation downstream of Mount Rainier, Washington, *U.S. Geol. Surv. Numbered Ser. 2012–1242, USGS, Reston, VA, Open-File Report*, 1–134 p.

Davis, P. (2024). Development and operation of a Global-Scale Seismographic Network: The IRIS/USGS GSN, *Perspect.*

Earth Space **5,** no. 1, e2023CN000225, doi: 10.1029/2023CN000225.

Farin, M., V. C. Tsai, M. P. Lamb, and K. E. Allstadt (2019). A physical model of the high-frequency seismic signal generated by debris flows, *Earth. Surf. Process. Landf.* **44,** no. 13, 2529–2543, doi: 10.1002/esp.4677.

Farrell, J., S. Wu, K. M. Ward, and F. Lin (2018). Persistent noise signal in the Fairfield nodal three-component 5-Hz geophones, *Seismol. Res. Lett.* **89,** no. 5, 1609–1617, doi: 10.1785/0220180073.

Gardner, G. H. F., L. W. Gardner, and A. R. Gregory (1974). Formation velocity and density; the diagnostic basics for stratigraphic traps, *Geophysics* **39,** no. 6, 770–780, doi: 10.1190/1.1440465.

Gimbert, F., V. C. Tsai, and M. P. Lamb (2014). A physical model for seismic noise generation by turbulent flow in rivers, *J. Geophys. Res. Earth Surf.* **119,** no. 10, 2209–2238, doi: 10.1002/2014JF003201.

Google (n.d.). [Google Earth imagery of Tahoma Creek channel, 26 July 2021], available at https://earth.google.com/web/@46.7976025,-121.87738951,1014.23172049a,352.21906082d,35y,219.99958037h,0t,0r/ (last accessed December 2025).

Guedes, V. J. C. B., S. T. R. Maciel, and M. P. Rocha (2022). Refrapy: A Python program for seismic refraction data analysis, *Comput. Geosci.* **159,** 105020, doi: 10.1016/j.cageo.2021.105020.

Havskov, J., and G. Alguacil (2016). *Instrumentation in Earthquake Seismology*, Springer, Cham, doi: 10.1007/978-3-319-21314-9.

Hungr, O., S. G. Evans, M. J. Bovis, and J. N. Hutchinson (2001). A review of the classification of landslides of the flow type, *Environ. Eng. Geosci.* **7,** no. 3, 221–238, doi: 10.2113/gseegeosci.7.3.221.

Hürlimann, M., V. Coviello, C. Bel, X. Guo, M. Berti, C. Graf, J. Hübl, S. Miyata, J. B. Smith, and H.-Y. Yin (2019). Debris-flow monitoring and warning: Review and examples, *Earth Sci. Rev.* **199,** 102981, doi: 10.1016/j.earscirev.2019.102981.

Iverson, R. M. (1997). The physics of debris flows, *Rev. Geophys.* **35,** no. 3, 245–296, doi: 10.1029/97RG00426.

Jakob, M., and O. Hungr (2005). *Debris-Flow Hazards and Related Phenomena*, Springer, Berlin, New York.

Jolly, A. D., L. Chardot, J. Neuberg, N. Fournier, B. J. Scott, and S. Sherburn (2012). High impact mass drops from helicopter: A new active seismic source method applied in an active volcanic setting, *Geophys. Res. Lett.* **39,** no. 12, 2012GL051880, doi: 10.1029/2012GL051880.

Kean, J. W., J. A. Coe, V. Coviello, J. B. Smith, S. W. McCoy, and M. Arattano (2015). Estimating rates of debris flow entrainment from ground vibrations, *Geophys. Res. Lett.* **42,** no. 15, 6365–6372, doi: 10.1002/2015GL064811.

Kramer, R. L., W. A. Thelen, A. M. Iezzi, S. C. Moran, and B. A. Pauk (2024). Recent expansion of the Cascades volcano observatory geophysical network at Mount Rainier for improved volcano and Lahar monitoring, *Seismol. Res. Lett.* **95,** no. 5, 2707–2721, doi: 10.1785/0220240112.

Lai, V. H., V. C. Tsai, M. P. Lamb, T. P. Ulizio, and A. R. Beer (2018). The seismic signature of debris flows: Flow mechanics and early warning at Montecito, California, *Geophys. Res. Lett.* **45,** no. 11, 5528–5535, doi: 10.1029/2018GL077683.

Marchi, L., V. Coviello, and M. Hürlimann (2024). Warning systems and instrumentation, in *Advances in Debris-Flow Science and Practice*,M. Jakob, S. McDougall, and P. Santi (Editors), Springer International Publishing, Cham, Geoenvironmental Disaster Reduction, 589–610, doi: 10.1007/978-3-031-48691-3_18.

Park, C. B., R. D. Miller, and J. Xia (1999). Multichannel analysis of surface waves, *Geophysics* **64,** no. 3, 800–808, doi: 10.1190/1.1444590.

Petrosino, S., P. Cusano, G. Saccorotti, and E. Del Pezzo (2002). Seismic attenuation and shallow velocity structures at Stromboli volcano, Italy, *Bull. Seismol. Soc. Am.* **92,** no. 3, 1102–1116, doi: 10.1785/0120010147.

Piantini, M., F. Gimbert, M. Bakker, A. Recking, and U. Nanni (2022). Using a dense seismic array to study fluvial processes in a braided river reach under flood conditions, *LHB* **108,** no. 1, 2053314, doi: 10.1080/27678490.2022.2053314.

Ringler, A. T., R. E. Anthony, M. S. Karplus, A. A. Holland, and D. C. Wilson (2018). Laboratory tests of three Z-land Fairfield Nodal 5-Hz, three-component sensors, *Seismol. Res. Lett.* **89,** no. 5, 1601–1608, doi: 10.1785/0220170236.

Sambridge, M. (1999). Geophysical inversion with a neighbourhood algorithm—I. Searching a parameter space, *Geophys. J. Int.* **138,** no. 2, 479–494, doi: 10.1046/j.1365-246X.1999.00876.x.

Scheidegger, A. E., and P. L. Willmore (1957). The use of a least squares method for the interpretation of data from seismic surveys, *Geophysics* **22,** no. 1, 9–21, doi: 10.1190/1.1438348.

Schimmel, A., V. Coviello, and F. Comiti (2022). Debris flow velocity and volume estimations based on seismic data, *Nat. Hazard. Earth Syst. Sci.* **22,** no. 6, 1955–1968, doi: 10.5194/nhess-22-1955-2022.

Shearer, P. M. (2009). *Introduction to Seismology*, Cambridge University Press, Cambridge, doi: 10.1017/CBO9780511841552.

Smith, T. J., J. S. Steinhart, and L. T. Aldrich (1966). Lake Superior crustal structure, *J. Geophys. Res.* **71,** no. 4, 1141–1172, doi: 10.1029/JZ071i004p01141.

Totman, M. E., M. E. Swanson, T. M. Rodgers, P. A. McDaniel, R. A. Rupp, and D. J. Brown (2014). Soil organic carbon stocks in the forests of Mount Rainier National Park, Washington, *Soil Sci. Soc. Am. J.* **78,** no. S1, doi: 10.2136/sssaj2013.08.0374nafsc.

Tsai, V. C., B. Minchew, M. P. Lamb, and J. Ampuero (2012). A physical model for seismic noise generation from sediment transport in rivers, *Geophys. Res. Lett.* **39,** no. 2, 2011GL050255, doi: 10.1029/2011GL050255.

Vallance, J. W. (2005). Volcanic debris flows, in *Debris-Flow Hazards and Related Phenomena*,M. Jakob and O. Hungr (Editors), Praxis Publishing Ltd, Chichester, United Kingdom, 247–274.

Vantassel, J. (2022). jpvantassel/swprepost: v2.0.0, *Zenodo*, doi: 10.5281/ZENODO.3839998.

Vantassel, J. (2024). jpvantassel/swprocess: v0.3.0, *Zenodo*, doi: 10.5281/ZENODO.4584128.

Vantassel, J. P., and B. R. Cox (2020). SWinvert: A workflow for performing rigorous 1-D surface wave inversions, *Geophys. J. Int.* **224,** no. 2, 1141–1156, doi: 10.1093/gji/ggaa426.

Vantassel, J. P., and B. R. Cox (2022). SWprocess: A workflow for developing robust estimates of surface wave dispersion uncertainty, *J. Seismol.* **26,** no. 4, 731–756, doi: 10.1007/s10950-021-10035-y.

Walder, J. S., and C. L. Driedger (1995). Frequent outburst floods from South Tahoma Glacier, Mount Rainier, U.S.A.: Relation to debris flows, meteorological origin and implications for subglacial hydrology, *J. Glaciol.* **41,** no. 137, 1–10, doi: 10.3189/S0022143000017718.

Wathelet, M. (2008). An improved neighborhood algorithm: Parameter conditions and dynamic scaling, *Geophys. Res. Lett.* **35,** no. 9, 2008GL033256, doi: 10.1029/2008GL033256.

Wathelet, M., J.-L. Chatelain, C. Cornou, G. D. Giulio, B. Guillier, M. Ohrnberger, and A. Savvaidis (2020). Geopsy: A user-friendly open-source tool set for ambient vibration processing, *Seismol. Res. Lett.* **91,** no. 3, 1878–1889, doi: 10.1785/0220190360.

Wathelet, M., D. Jongmans, and M. Ohrnberger (2005). Direct inversion of spatial autocorrelation curves with the neighborhood algorithm, *Bull. Seismol. Soc. Am.* **95,** no. 5, 1787–1800, doi: 10.1785/0120040220.

Wessel, P., W. H. F. Smith, R. Scharroo, J. Luis, and F. Wobbe (2013). Generic Mapping Tools: Improved version released, *EoS Trans.* **94,** no. 45, 409–410, doi: 10.1002/2013EO450001.

Willmore, P. L., and A. M. Bancroft (1960). The time term approach to refraction seismology, *Geophys. J. Int.* **3,** no. 4, 419–432, doi: 10.1111/j.1365-246X.1960.tb01715.x.

Witham, C. S. (2005). Volcanic disasters and incidents: A new database, *J. Volcanol. Geotherm. Res.* **148,** nos. 3/4, 191–233, doi: 10.1016/j.jvolgeores.2005.04.017.

Zhang, Z., F. Walter, B. W. McArdell, M. Wenner, M. Chmiel, T. De Haas, and S. He (2021). Insights from the particle impact model into the high-frequency seismic signature of debris flows, *Geophys. Res. Lett.* **48,** no. 1, e2020GL088994, doi: 10.1029/2020GL088994.

Manuscript received 26 February 2025
Published online 17 March 2026